



Surface micro-texture and tribological properties in longitudinal-torsional ultrasonic-assisted milling Ti_2AlNb

Ziwen Xia^{1,2,3} · Guofu Gao⁴ · Yi Wang⁴ · Menghua Zhang^{1,2,3} · Fangchao Jia^{1,2,3} · Chenwei Shan^{1,2,3}

Received: 10 November 2022 / Accepted: 2 March 2023 / Published online: 16 March 2023
© The Author(s), under exclusive licence to Springer-Verlag London Ltd., part of Springer Nature 2023

Abstract

Ti_2AlNb has much application potential in the aerospace sector thanks to its outstanding material characteristics. Poor wear resistance, however, blocks its development. This study used LTUAM (longitudinal-torsional ultrasonic-assisted milling) to get the surface micro-texture of Ti_2AlNb in order to address the issue. By comparing traditional milling (CM), the surface micro-texture and tribological characteristics were studied. On this basis, the kinematic characteristics of the elliptical vibration were explored, introducing the critical condition of the separated pattern. In addition, the torsion-rotation ratio was put forward to understand the separation characteristics. The corresponding finite element model exhibited these kinematic characteristics. The model also looked into how the cutting parameters affected the way surface microtexture was generated. Experimental results indicated that machined surfaces with uniform micro-texture were seen in LTUAM, whereas scratches predominated in CM. The variation of micro-texture and surface roughness was discussed in respect to cutting parameters. It has been demonstrated that a machined surface with uniform micro-texture had superior tribological properties. The friction coefficient under LTUAM was approximately 27.08% less than that in CM.

Keywords Ti_2AlNb · Surface micro-texture · Tribological properties · Longitudinal-torsional ultrasonic-assisted milling · Separation characteristics

1 Introduction

The aero-engine materials emphasize low weight, high strength, and high-temperature resistance. Ti_2AlNb , a TiAl intermetallic alloy, is capable of meeting these requirements above. Because of its order orthorhombic crystal structure, it has a low density (about 60% of superalloys), excellent high-temperature resistance (work temperature over 200 °C than titanium alloys), and better creep resistance [1–3]. Since its inception, it has been regarded as the first-class material to serve aero-engine. However, its poor wear resistance prevents it from being applied [4], especially in aero-engines and gas turbines.

Multiple studies suggested that surfaces with micro-texture can improve their wear resistance [5, 6]. Surface micro-texture is typically obtained through laser [7], chemical etching [8], vapor deposition [9], vibration cutting [10], etc. Vibration cutting, a new cutting technology in which vibrations motivate the tool to cut (more than 20 kHz), has simple equipment and high processing efficiency. Micro-texture is completed as soon as the material is removed. As a result, no additional processing is required, but the vibration

✉ Chenwei Shan
shancw@nwpu.edu.cn

Ziwen Xia
605960053@qq.com

Guofu Gao
gaogf@hpu.edu.cn

Yi Wang
112005010001@home.hpu.edu.cn

Menghua Zhang
84284310@qq.com

¹ Key Laboratory of High Performance Manufacturing for Aero Engine, Ministry of Industry and Information Technology, Northwestern Polytechnical University, Xi'an 710072, China

² Engineering Research Center of Advanced Manufacturing Technology for Aero Engine, Ministry of Education, Northwestern Polytechnical University, Xi'an 710072, China

³ State Key Laboratory of Cemented Carbide, Zhuzhou Hunan 412000, China

⁴ School of Mechanical and Power Engineering, Henan Polytechnic University, Jiaozuo 454000, China

system stability is critical. It is an extremely promising cutting method. Liu et al. [11] believed that using ultrasonic vibration turning (UVT) to obtain the surface micro-texture of copper could be a low-cost and high-effective method of surface micro-texture. Amini et al. [12] also conducted a wear test on the surface micro-texture under UVT. In terms of friction coefficient and wear rate, there is a significant improvement. In addition, vibration cutting has achieved remarkable results for difficult-to-cut materials [13–15]. Lower cutting forces, tool wear, and better surface integrity are all possible [16–18]. Regretfully, there is no relevant information available in Ti_2AlNb .

Ti_2AlNb advances the application stage slowly. Material machining technology, in addition to material development, faces enormous challenges. Such materials with low thermal conductivity, high chemical activity, and strength are considered difficult to cut. Accordingly, during machining, fast tool wear, high cutting force and temperature, and poor surface quality are common [19]. Researchers dedicate to developing special machining techniques to overcome these obstacles, such as high-speed machining (HSM) [20], cryogenics cutting (CC), and minimal quantity lubrication (MQL) [21]. These machining methods are either softening the material at high temperatures or at low temperatures to suppress the wear rates of tools. In fact, problem-solving is not comprehensive. HSM allows for ductile-domain cutting of brittle materials, but the tool wears out quickly. Although CC effectively reduces the cutting temperature and tool wear, micro-cracks may be occurred because of the steep temperature. Accordingly, ultrasonic vibration cutting has great potential for machining Ti_2AlNb .

At present, available publications have demonstrated its poor machinability. Xi et al. [22] compared the grinding performance of Ti_2AlNb with Ti-6Al-4 V and Inconel 718. They discovered that the white layers of Ti_2AlNb occurred more easily than the reference substances. Following that, Xi et al. [19] investigated its surface quality further. Increasing the material removal rate resulted in a thicker white layer. The work of Sim et al. [23] reported the removal mechanism of Ti_2AlNb . As α_2 is the brittle phase, it is removed first. Thus, some microcracks may occur during this stage. As the tool advances, such surface defects will be introduced into the material matrix, causing additional damage. In other ways, recrystallization was observed under 0.3 mm grinding depth, and α_2 and O phases disappeared meanwhile. Except for cracks and voids, grinding burns caused by severe mechanical-thermal loads also should be avoided. Information about vibration machining, Yuan et al. [24] designed a plane vibration platform for milling Ti_2AlNb in the way of workpiece vibration. Better machined surfaces were observed in vibration milling rather than CM. Bhaduri et al. [25] investigated the ultrasonic grinding performance of γ -TiAl (one branch of TiAl intermetallic alloys),

demonstrating the desirable results in terms of forces and surface defects.

More evidence suggests that the finite element method (FEM) is a good way to observe what happens in the cutting zone [26–28], wherein the material constitutive model (MCM) was considered the critical factor affecting model error. To accurately describe the actual deformation behavior, He et al. [21] proposed an MCM of Ti_2AlNb based on the inverse identification method. The model is based on the TANH structure (a modified J–C model), which has been shown to accurately describe the flow stress during cutting. Afterward, the model was applied to simulate the process of high-pressure jet coolant cutting Ti_2AlNb [29].

Regarding these problems above, this study applied LTUAM to obtain the surface micro-texture of Ti_2AlNb , with the goal of improving wear resistance and machinability. To further study the generation mechanism of the surface micro-texture, the kinematic characteristics of LTUAM were analyzed deeply. And FEM visualization supported these theories by explaining the generation mechanism of surface micro-texture. It has the potential to increase the potential of FEM in multiple-dimensional ultrasonic machining. Finally, the surface morphology and its tribological properties were discussed, and conclusions were presented.

2 Kinematic analysis of LTUAM

2.1 Periodic motion characteristics of LTUAM

The vibration system of LTUAM is depicted in Fig. 1. The reason why the tool moves in the elliptical type is attributed to the self-designed horn with helical grooves. The horn can amplify the longitudinal vibration resulting from the transducer and transform it into the torsional pattern partly. By the converse piezoelectric effect, the transducer is to convert the externally excited electrical power (from the ultrasonic generator) into mechanical vibration. For rotary ultrasonic machining, the electrical energy transmits to the transducer by means of the wireless transmission device. The device consists of two induction coils in which the transmitting terminal is fixed on the spindle frame and the receiving terminal is set inside the ultrasonic holder. Thus, for the single excitation source, the two vibration types are of the same frequency.

The tool coordinate system o - xyz was established based on the milling end origin, as shown in Fig. 1, where x , y , and z represent the tool feed, normal and longitudinal vibration directions, respectively.

For the rotational motion of the tool on the xoy plane, it is the superposition both in spindle rotation and torsional vibration. One point of the tool nose rotates by angle θ and

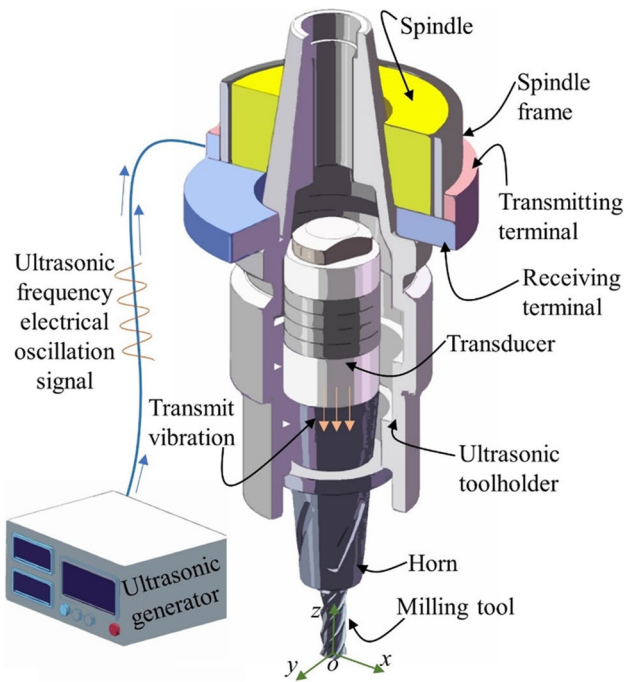


Fig. 1 Vibration system of LTUAM

arc S during time Δt . Therefore, the linear velocity v_s and arc length of the tool nose were given by

$$v_s = v_c + v_u = 2\pi \left[\frac{nr}{60} + fA_t \cos(2\pi ft) \right] \quad (1)$$

$$S = \int_t^{t+\Delta t} v_s dt \quad (2)$$

where r is the tool radius (mm), n is the spindle speed (r/min), v_c is the linear velocity result from spindle rotation (m/s), v_u is

the linear velocity result from torsional vibration (m/s), f is the ultrasonic frequency (kHz), and A_t is the vibration amplitude (μm) of torsional vibration respectively.

And then, the rotation angle θ of LTUAM can be expressed as

$$\theta = \frac{S}{r} \quad (3)$$

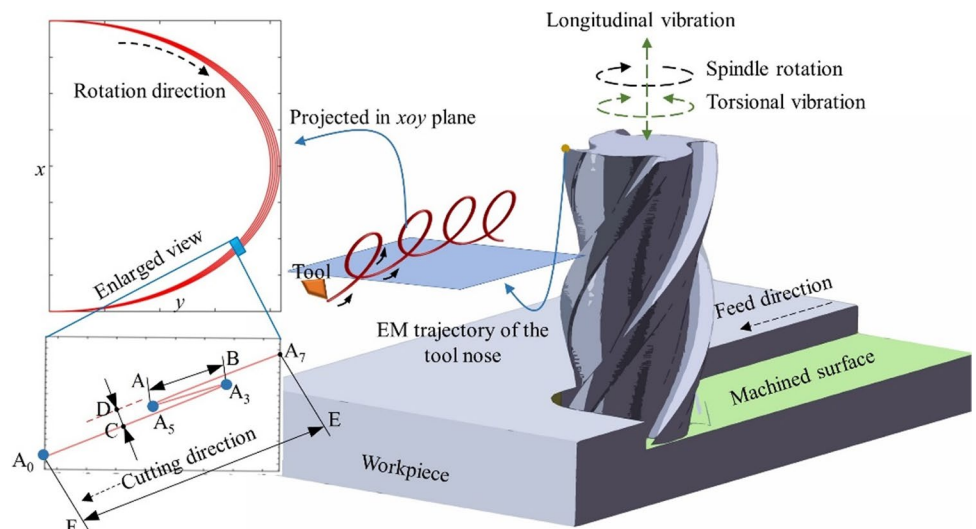
The trajectory equation of LTUAM was presented as

$$\begin{cases} x(t) = r \sin \left[\frac{2\pi nt}{60} + \frac{A_t \sin(2\pi ft)}{r} + \frac{2\pi i}{N} \right] + \frac{v_f t}{60} \\ y(t) = r \cos \left[\frac{2\pi nt}{60} + \frac{A_t \sin(2\pi ft)}{r} + \frac{2\pi i}{N} \right] \\ z(t) = A_l \sin(2\pi ft + \varphi) \end{cases} \quad (4)$$

where A_l is the longitudinal amplitude (μm), N is the number of milling teeth, i is the i -th tooth, φ is the phase difference (rad), and v_f is the feed speed (mm/min).

Based on the discussion above, the EM pattern of LTUAM can be obtained as shown in Fig. 2. Apparently, the torsional vibration was on the xoy plane, and the longitudinal vibration was along the tool axial. This type of motion trajectory may cause the tool to leave the cutting zone. Studies have shown that this alleviates the bad environment of the zone [30, 31]. The vibration amplitude along the cutting direction has the greatest influence on separation ability. Assume the tool nose moves from point F to point E during the vibration period. The xoy plane projection of tool retraction caused by torsional vibration is from B to A (denoted as retraction distance). At this time, the direction of the torsional vibration velocity is opposite to the direction of the rotational velocity. The tool feed also causes the line segment DC.

Fig. 2 Tool nose motion trajectory of LTUAM



2.2 Separation characteristics of LTUAM

The cutting plane view of the tool during cutting is presented in Fig. 3. The tool follows the EM trajectory to cut materials. Because of the tool intrusion into the workpiece, the machined surface will produce regular and uniform micro-texture. During a given vibration period, let A_0 be the starting point and A_7 be the ending point. The tool cutting path is A_0 - A_1 - A_2 - A_3 - A_4 - A_5 - A_6 - A_7 . From A_2 to A_3 , v_u is negative (opposed to v_c), and the corresponding acceleration a_u is also negative, resulting in v_u increasing. At this stage, v_u is still less than v_c , thereby v_s is still positive. As a result, the tool works in the cutting direction but at a slower speed until it reaches the switching position A_3 ($v_u = -v_c$). At the time, the tool is at a position of maximum tangential contact with the workpiece and soon separates against the cutting zone. The view of these special points on the xoy plane is shown in Fig. 2, and the spatial position of Fig. 3 can be seen by superimposing the longitudinal vibration finally.

In the following stage (A_3 to A_4), v_u exceeds v_c . Since a_u is in the same direction as v_u , the tool accelerates to separate against the cutting zone. After reaching A_4 , a_u becomes positive and v_u begins to reduce. The separated speed is weakened until the tool reaches A_5 . From A_3 to A_5 , v_u is always greater than v_c but in the opposite direction. In the balance point A_5 ($-v_u = v_c$), the tool is toward the cutting direction. In fact, cutting does not begin until the tool reaches A_1 again (denote as $A_{1/a}$). It is due to A_5 - A_1 being included in the cutting area during A_1 - A_3 . Therefore, the actual cutting path is $A_{1/a}$ - A_7 - A_8 of any vibration period. A_3 - A_5 is the separated path. And the vacancy cutting path is A_3 - A_4 - A_5 - $A_{1/a}$, wherein A_7 , A_8 , and A_9 are the points of the next vibration period, which are parallel to A_0 , A_3 , and A_5 , respectively. As a result, the dynamic cutting speeds during the separated EM cutting can be expressed by Eq. (5).

$$v_s = \begin{cases} v - |2\pi f A_t \cos(2\pi f t)| \geq 0, & t_{A_0} + zT < t < t_{A_3} + zT \\ v - |2\pi f A_t \cos(2\pi f t)| \leq 0, & t_{A_3} + zT < t < t_{A_4} + zT \\ v + |2\pi f A_t \cos(2\pi f t)| \leq 0, & t_{A_4} + zT < t < t_{A_5} + zT \\ v + |2\pi f A_t \cos(2\pi f t)| \geq 0, & t_{A_5} + zT < t < t_{A_7} + zT \end{cases} \quad (5)$$

While for the unseparated type, it can be given by

$$v_s = \begin{cases} v - |2\pi f A_t \cos(2\pi f t)| \geq 0, & t_{A_0} + zT < t < t_{A_4} + zT \\ v + |2\pi f A_t \cos(2\pi f t)| \geq 0, & t_{A_4} + zT < t < t_{A_7} + zT \end{cases} \quad (6)$$

where T is the vibration period, $z=0, 1, 2, \dots$,

As mentioned above, the moment the tool reached the switching point was

$$t_s = \frac{\arccos(-\frac{nr}{60fAt})}{2\pi f} + zT \quad (7)$$

And the separated time within a vibration period was given by

$$t_{se} = \frac{\pi - \arccos(-\frac{nr}{60fAt})}{\pi f} \quad (8)$$

Only if the following condition is met does the switching point exist,

$$\frac{nr}{60fAt} < 1 \quad (9)$$

It can be seen as a critical condition for the separated EM trajectory. Increasing frequency and amplitude are in favor of the ultrasonic separation ability. As these parameters far meet Eq. (9), the separated time lengthens, implying that the more obvious the EM trajectory, the better the separation ability. While the cutting parameters are not satisfied with the critical condition, the unseparated EM trajectory occurred. Although the tool loses the separated ability, the dynamic cutting thickness resulting from ultrasound still

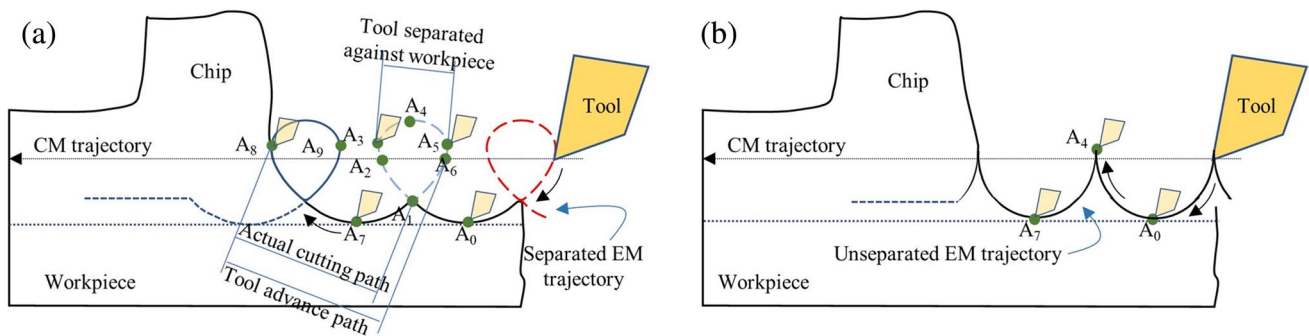


Fig. 3 Two EM trajectories of LTUAM, (a) separated EM trajectory; (b) unseparated EM trajectory

aids in cutting. This is common in high-speed ultrasonic-assisted milling or single-direction vibration patterns [32].

In accordance with Eq. (8), Fig. 4 depicts the separated time and the critical point. In Fig. 4(a), increasing vibration amplitude leads to prolonging separated time. While increasing speed necessitates larger vibration amplitudes to maintain a constant separated time. The important point to remember is that, as shown in Fig. 4(b), no matter how large the amplitude increases, the separation time will eventually converge to an upper bound, close to $1/2f$. Figure 4(c) and (d) show that increasing speed relates negatively to the separated time. Increasing vibration amplitudes also aid in raising the upper limit of the separation point at high speeds. When the speed is as low as possible, the separation time will converge to a bound.

Accordingly, the main factors influencing the separation ability are considered the acoustic parameters in the cutting direction (including f and A_t) and the spindle speed. The torsion-rotation ratio (TRR) was proposed to understand the influence of cutting parameters on the EM trajectory. It was defined as the circular displacement caused by torsional vibration in unit time as a percentage of rotation,

$$\xi = \frac{30A_t \sin(2\pi ft)}{\pi n r t} \tag{10}$$

The effect law of machining parameters on the TRR is shown in Fig. 5. The decay rate represents the degree to which the tool separation characteristics have weakened. In Fig. 5A, a positive correlation can be seen between the

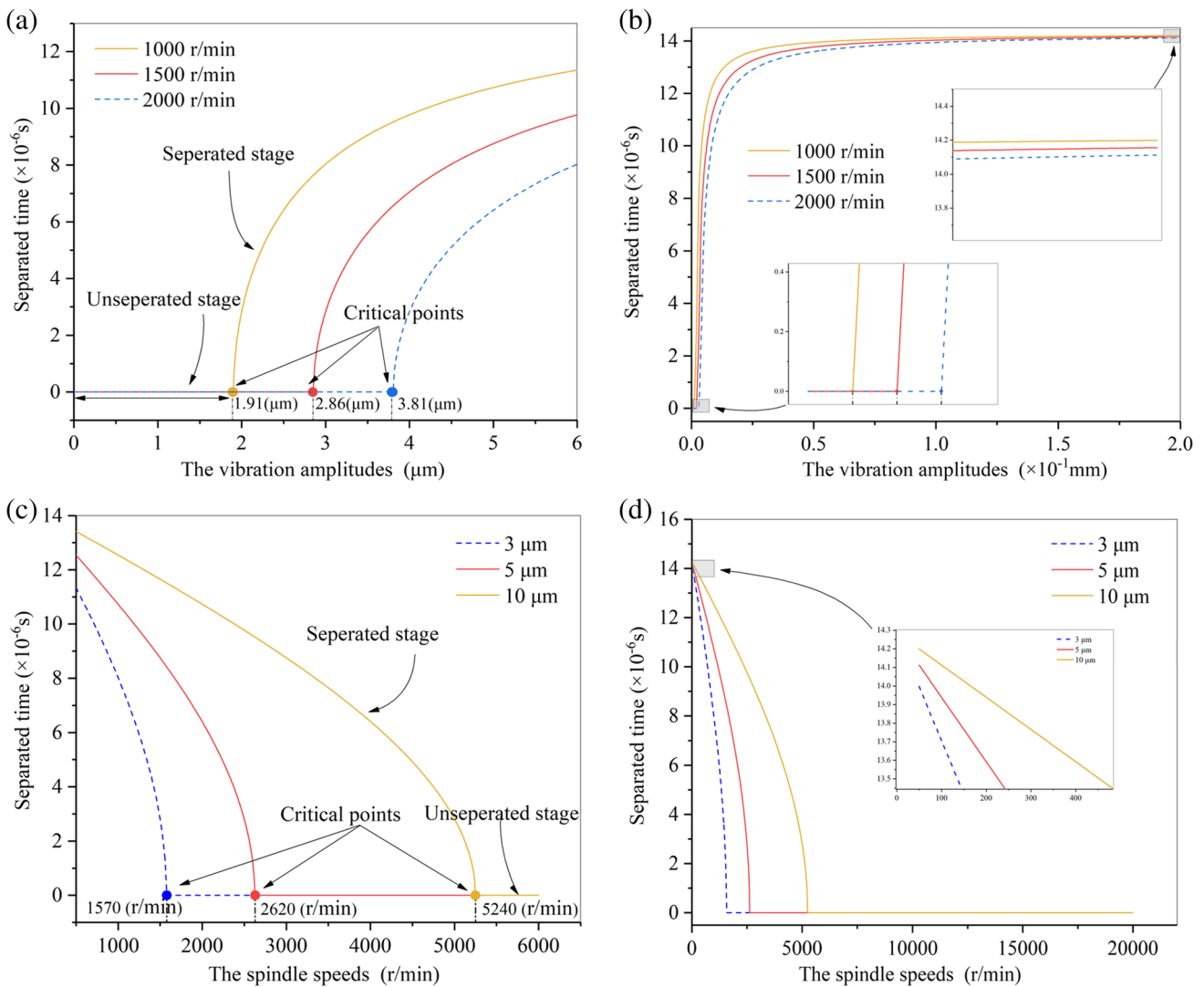


Fig. 4 Visualization of the separated time and the critical points, (a) and (b) are the influence vibration amplitudes on separated time in which (a) is in general condition and (b) is in enormous amplitudes;

(c) and (d) are the influence spindle speed on separated time in which (c) is in general condition and (d) is in high speed

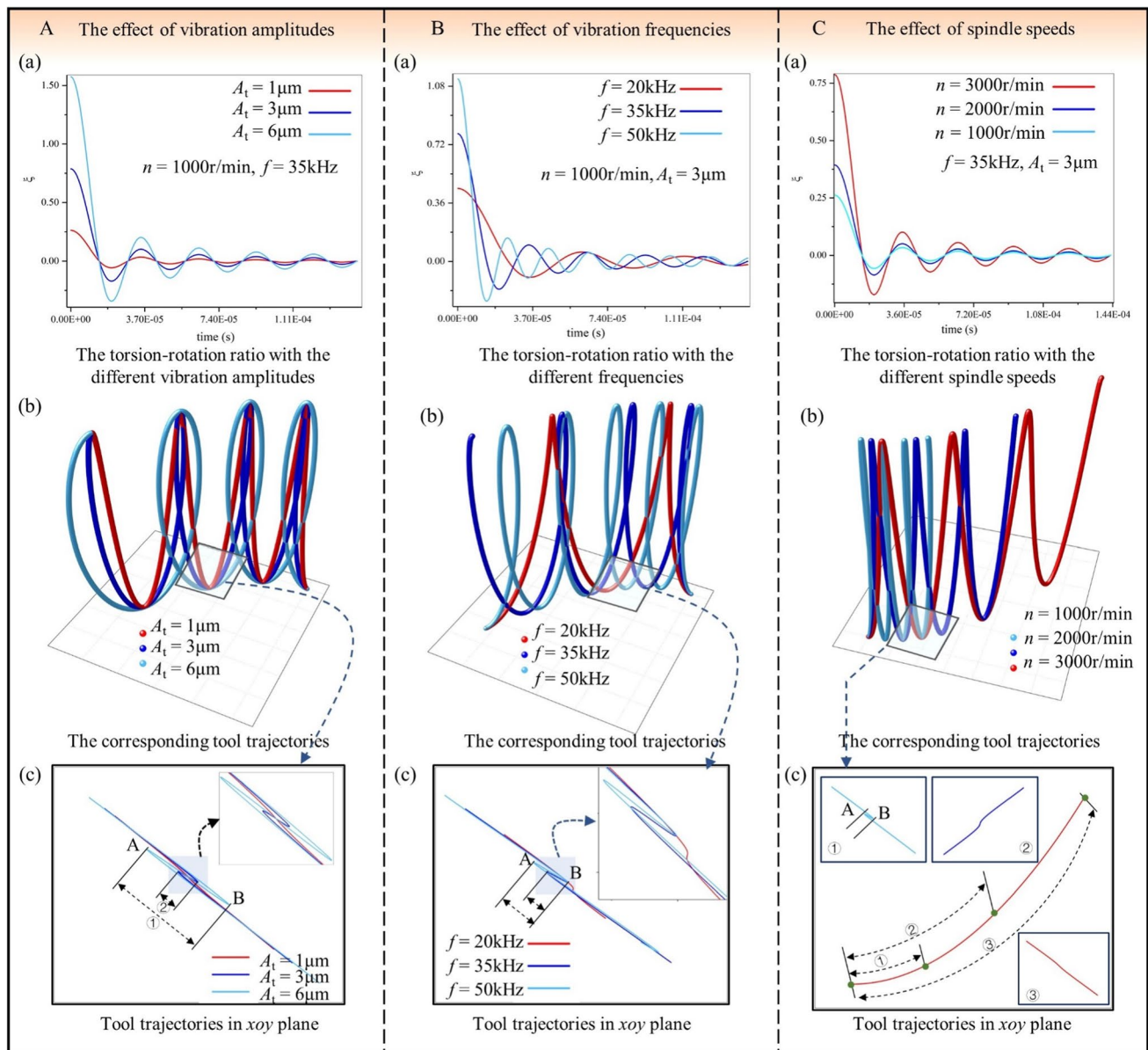


Fig. 5 Influence of cutting parameters on the EM trajectory

vibration amplitudes and TRR. As the spindle speed and vibration frequency are fixed, increasing the vibration amplitudes can enhance the vibration effect in the cutting direction. It means that the retraction distance AB will be longer, as shown in Fig. 5A(c), as well as the obvious EM trajectory. However, AB is not observed as $A_t = 1 \mu\text{m}$. Indeed, it also does not meet the critical condition. Figure 5B presents the effect of vibration frequency on TRR. The decay rate is slowed as the frequency increases. The increase in the number of vibrations per unit time leads to an increase in the retraction distance per unit time, which relatively improves the effect of elliptical motion. The cutting speed caused by torsional vibration is difficult to break through the rotation

speed as the spindle speed. Accordingly, the EM trajectory retraction distance will be significantly reduced.

The retreat distance of the EM trajectory at 1000 r/min is shown in Fig. 5C(c). When the speed reached 2000 r/min, the distance almost vanished, and the unseparated EM trajectory appeared, as shown in Fig. 5C(b). Furthermore, the separation effect caused by torsional vibration is rare. The vibration component (vibration number within the unit cutting distance) will be weakened as the spindle speed increases, causing the unit cutting distance to increase per unit time.

To achieve elliptical vibration separation, the critical condition must be satisfied as much as possible.

Nonetheless, in practical production, the proper cutting parameters must be considered. Hence, the resonant frequency and output power of the ultrasonic system must be designed in accordance with the cutting parameters.

2.3 Investigating the generation mechanism of surface micro-texture

The variable cutting thickness of LTUAM causes the micro-texture on the machined surface. Changes in cutting parameters cause different EM trajectories, resulting in a diverse micro-texture. It is, however, difficult for the camera to capture the mechanism of surface microtexture generation. As a consequence, FEM was used to investigate the generation mechanism of surface micro-texture.

The FEM model of LTUAM Ti₂AlNb was established based on ABAQUS Explicit. The tool was regarded as a rigid body, while the workpiece was a plastic body. The oblique cutting model was chosen for microscopic observation. Additionally, the model was also built on the following assumptions.

- (1) Tool wear was not considered;
- (2) The physical field effects caused by the continuous cutting process were ignored;
- (3) The effect of cutting temperature on material phase transformation was ignored;
- (4) some factors, such as machine tool vibration, noise, and so on, were ignored.

TANH MCM takes strain softening into account on the basis of the J-C MCM, which can more accurately describe the deformation behavior of materials under large strain and high strain rate conditions. The LTUAM Ti₂AlNb FEM model employed TANH MCM, and its parameters refer to Ref. [21].

Although ABAQUS provides periodic magnitude functions to the user (see Eq. (9)), acoustic parameters are frequently considered as displacement to carry out, whereas cutting parameters are frequently imposed as velocity boundary conditions. These two distinct types of boundary conditions are coupled in one direction, resulting in boundary conditions that are in conflict. As a result, the key to resolving the conflict is to use the same type of load application.

$$a(t) = A_0 + \sum_{n=1}^N [A_n \cos \omega(t - t_0) + B_n \sin \omega(t - t_0)] \quad (11)$$

where A_0 is the initial amplitude; A_n and B_n are the amplitude of cosine and sin functions, respectively; t_0 is the initial time; and ω is the circle frequency.

Based on Eqs. (1) and (9), the compound rotation motion of LTUAM is expressed by the angular velocity ω_t ,

$$\omega_t = \frac{2\pi n}{60} + \frac{2\pi f A_t \cos(2\pi f t)}{r} \quad (12)$$

And the longitudinal vibration speed was

$$v_l = 2\pi f A_1 \sin(2\pi f t) \quad (13)$$

Table 1 shows the torsional and longitudinal vibration variables that correspond to Eq. (9). To verify its accuracy, the displacement of the tool nose in the x , y , and z directions was output and compared to the result obtained from Eq. (4) with the same parameters (see Fig. 6). The different global coordinate systems between FEM and kinematic model result in the difference in the coordinate axes. However, it is clear that the displacement of the two types is consistent.

Figure 7 presents the cutting process of LTUAM during a vibration period (in $n = 1000$ r/min, $f = 35$ kHz, $A_1 = 3 \mu\text{m}$, $A_t = 1.8 \mu\text{m}$), and the amplitudes resulted from experimental data. Each stage was marked on the EM trajectory. The tool cut into the workpiece can be seen from a to c. And the tool separated against the workpiece from d to f. The separated feature can be affirmed by the material stress field. From a to c, it can be seen that the maximum stress position (marked in red) is caused by tool extrusion of the workpiece. It vanished from d to f in Fig. 7 due to the tool being removed from the primary cutting zone. The tool cut into the workpiece again within f to h, but this time it is on the empty cutting stage because it was included in the previous cutting period. As a result, the finite element results backed up the discussion in Section 2.2.

The designed resonant frequency of the horn fluctuated within a narrow range in the actual processing. Therefore, the acoustic parameter only considered the effect of vibration amplitudes in the following discussion.

Figure 8 presents the cutting process under various spindle speeds, exhibiting the three cutting stages and their machined surface at each speed ($f = 35$ kHz, $A_1 = 3 \mu\text{m}$, $A_t = 1.8 \mu\text{m}$). Compared with CM, LTUAM could improve chip breaking capability. For CM, the chips flowed along the rake face and gradually curled, whereas the chip breaking can be seen in LTUAM, whatever separated type or unseparated one. The best chip breaking capability occurred at $n = 1000$ r/min. And the tool separated from the cutting zone. Because of the decreasing vibration component, the

Table 1 Boundary condition variables of LTUAM correspond to the amplitude function

| Types | $a(t)$ | A_0 | A_n | B_n | ω | t_0 | N |
|------------------------|------------|-------------|-----------------|--------------|----------|-------|-----|
| Longitudinal vibration | v_l | 0 | 0 | $2\pi f A_1$ | $2\pi f$ | 0 | 1 |
| Torsional vibration | ω_t | $2\pi n/60$ | $2\pi f A_t/60$ | 0 | $2\pi f$ | 0 | 1 |

Fig. 6 Comparing the tool trajectories between the kinematic model and FEM, (a) result from the kinematic model; (b) result from FEM

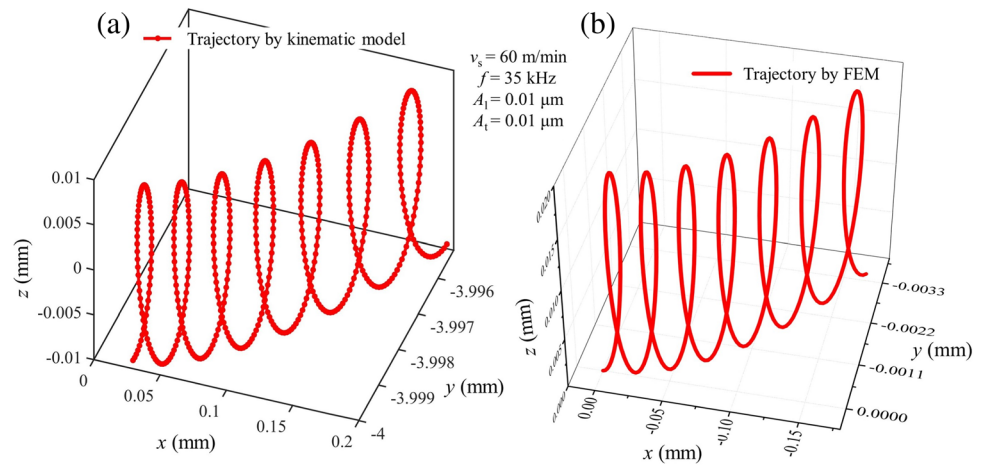
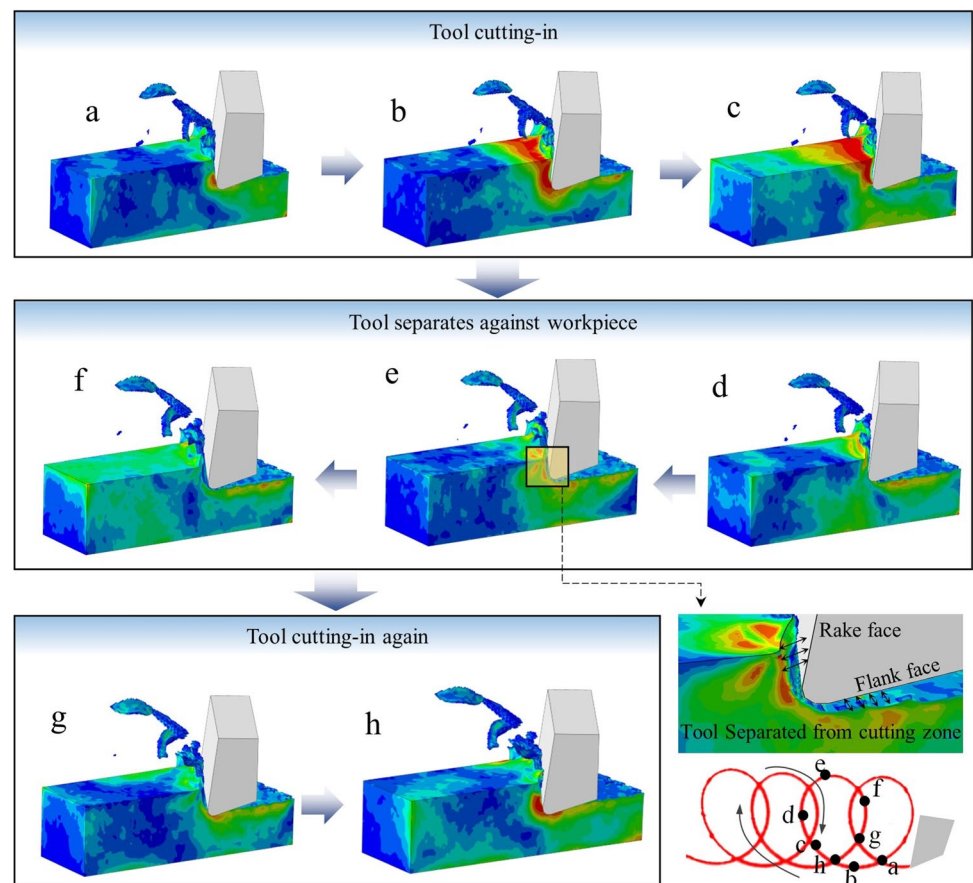


Fig. 7 Cutting process of LTUAM during a vibration period



phenomenon became weaker as the speed increased. Chip breaking relied on varying cutting thickness, which resulted in larger chip sizes and lower chip counts. It is clear from these machined surfaces that the flat surface occurred in CM while the uniform surface micro-texture occurred in LTUAM. As the spindle speed increased, the reducing vibration component also reduced the number of ironings of the flank face against the material surface. The density of the surface micro-texture per unit area was reduced while the micro-texture size was increased.

As shown in Fig. 9, the machined surface morphologies varied with the vibration amplitudes. The height of the micro-texture peak and valley was low due to the vibration amplitudes $A_1 = 1$ μm , $A_t = 0.67$ μm , and the characteristics of the micro-texture were not obvious. With the vibration amplitudes growing, the ironing effect of the flank face against the material surface was enhanced, thereby the significant micro-textures (see Fig. 9(b) and (c)). However, the overgrowing vibration amplitudes made the ironing degree over. It caused

Fig. 8 Machined surface states with different spindle speeds

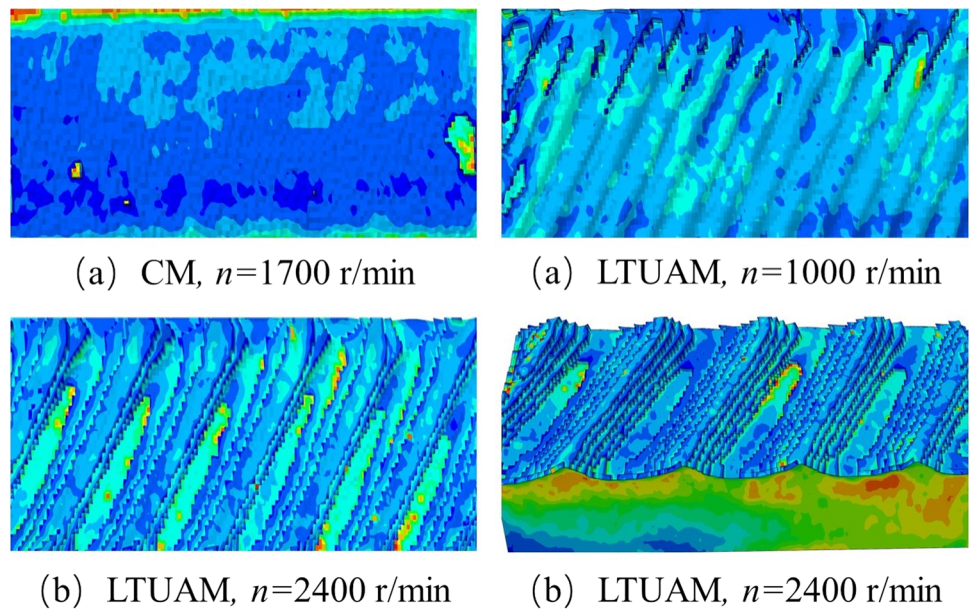
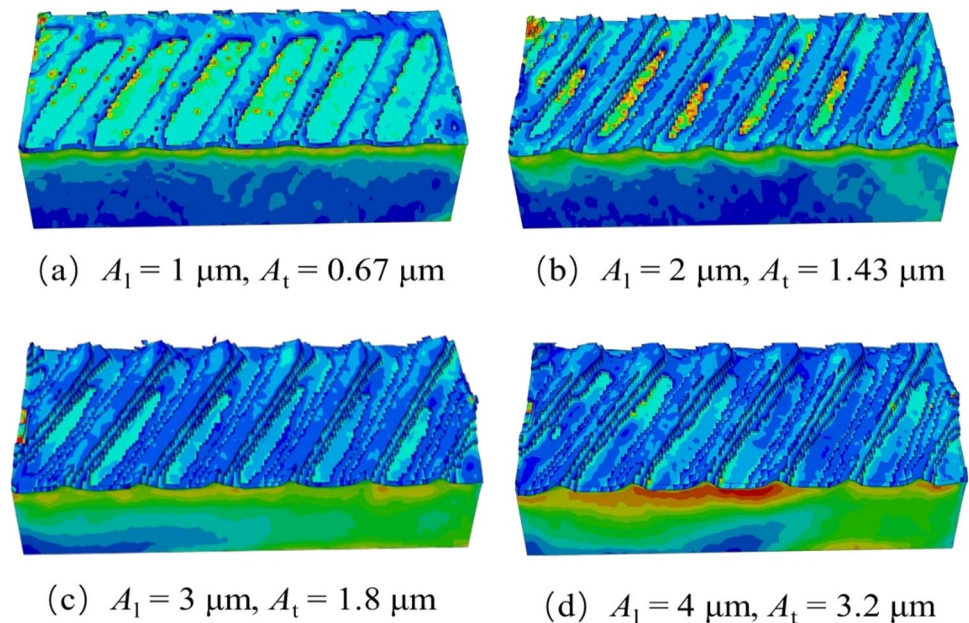


Fig. 9 Machined surface states of LTUAM with different vibration amplitudes



an increase in the slope of the microtexture, making them less noticeable than expected, as shown in Fig. 9(d).

3 Experimental details

In Fig. 10, the experiment of LTUAM Ti₂AlNb in dry cutting was performed on a vertical machining center VMC-850 based on the longitudinal-torsional composite

horn (designed resonant frequency 35 kHz) designed by half wavelength. The workpiece was O phase TiAl alloys Ti₂AlNb, Ti-22Al-24Nb-0.5Mo, at%. And the coated milling tools were employed. Tables 2 and 3 contain descriptions of their parameters. To analyze the influence of cutting parameters on surface microtexture, the detailed experiment scheme is presented in Table 4. Furthermore, the MWF-500, a friction and

Fig. 10 Experiment site of LTUAM Ti_2AlNb

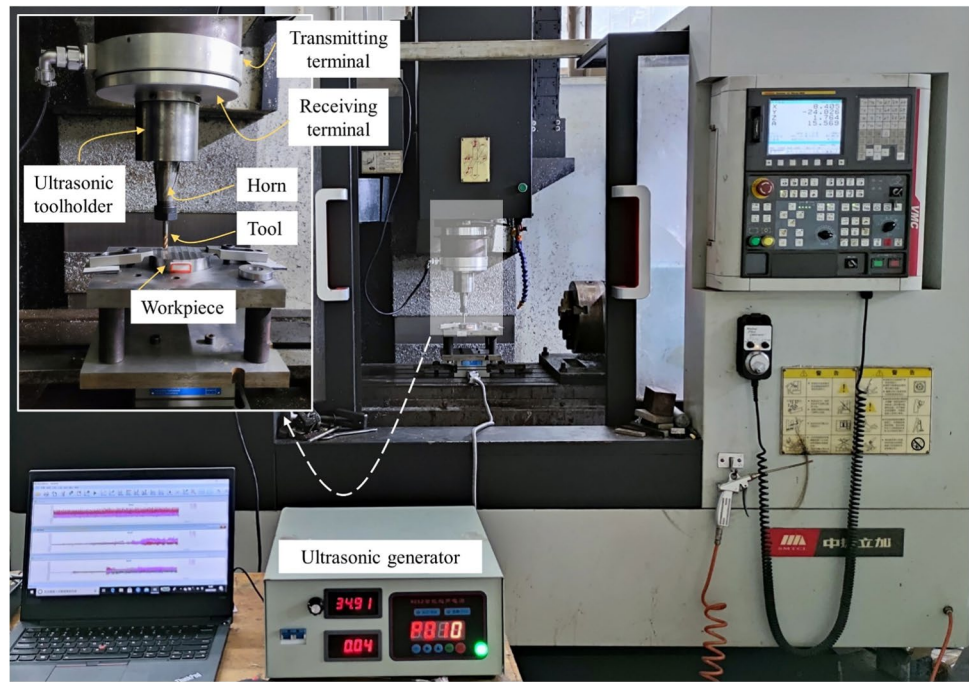


Table 2 Compositional analysis results of each element of Ti_2AlNb

| Elements | Al | Nb | Mo | Fe | Si | C | Ti |
|----------|-------|-------|------|-------|-------|-------|-----------|
| wt% | 10.0% | 41.5% | 0.9% | 0.04% | 0.03% | 0.15% | Remainder |

Table 3 Specifications of the milling cutter

| Material | Radius | Helix angle | Hardness | Cutter teeth | Blade length |
|----------------------|--------|-------------|----------|--------------|--------------|
| AlTiN-coated carbide | 4 mm | 30° | 65HRC | 4 | 20 mm |

wear reciprocating linear testing machine, was used for the corresponding friction and wear test.

The machined surface morphologies were observed by the digital microscope (Keyence VHX-2000, Japan). Their surface roughness was measured using a contour device (Bruker GTK, Germany). The vibration amplitudes were measured using a laser displacement sensor (Keyence LK-G10, Japan). Focusing on the tool end, the laser can identify the longitudinal displacement, whereas it was not suitable for torsional one. Accordingly, the torsional type can be measured by the transformation method [33]. The vibration amplitudes, both in the longitudinal direction and the torsional one, are listed in Table 4.

Table 4 Single-factor experiment scheme

| n (r/min) | A_l (μm) | A_t (μm) | f_r (mm/r) | f (kHz) | a_p (mm) |
|---------------------|-------------------------|-------------------------|--------------|-----------|------------|
| 1700 | 1/2/3/4 | 0.67/1.43/1.8/3.2 | 0.01 | 35 | 0.1 |
| 1000/1700/2400/3100 | 3 | 1.8 | 0.01 | 35 | 0.1 |

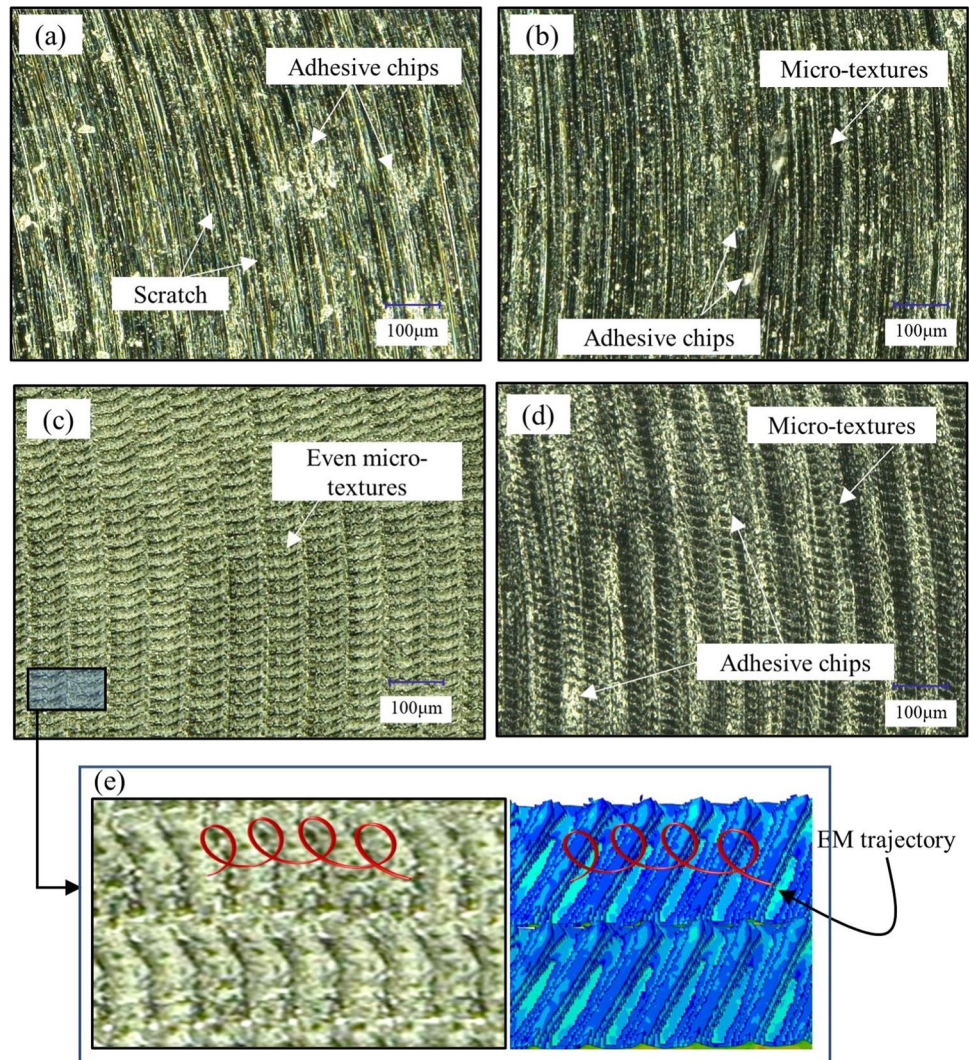
4 Results and discussion

4.1 Surface micro-texture morphologies

Figure 11 depicts the surface microtexture morphologies in both CM and LTUAM. It demonstrates completely different characteristics. The scratches caused by the cutting edge were dominant in CM. And numerous chips stuck to the machined surface. While in LTUAM, the phenomenon has been significantly improved. Along the EM trajectory advancing, the tool ironed the material surface at the ultrasonic frequency. Eventually, the surface micro-texture was formed.

Ti_2AlNb , as an intractable material, led to a larger cutting force and temperature during machining. The poor chip breaking ability of CM was solely dependent on the cut-in and cut-out of adjacent milling teeth. Additionally, the chemical activity of Ti and Al is active, and it is easy to adhere to the surface in dry cutting when the cutting temperature is too high. Therefore, the intermittent cutting process of LTUAM

Fig. 11 Surface micro-texture of LTUAM with different vibration amplitudes, (a) CM; (b) LTUAM, $A_t = 1 \mu\text{m}$, $A_t = 0.67 \mu\text{m}$; (c) LTUAM, $A_t = 3 \mu\text{m}$, $A_t = 1.8 \mu\text{m}$; (d) LTUAM, $A_t = 4 \mu\text{m}$, $A_t = 3.2 \mu\text{m}$



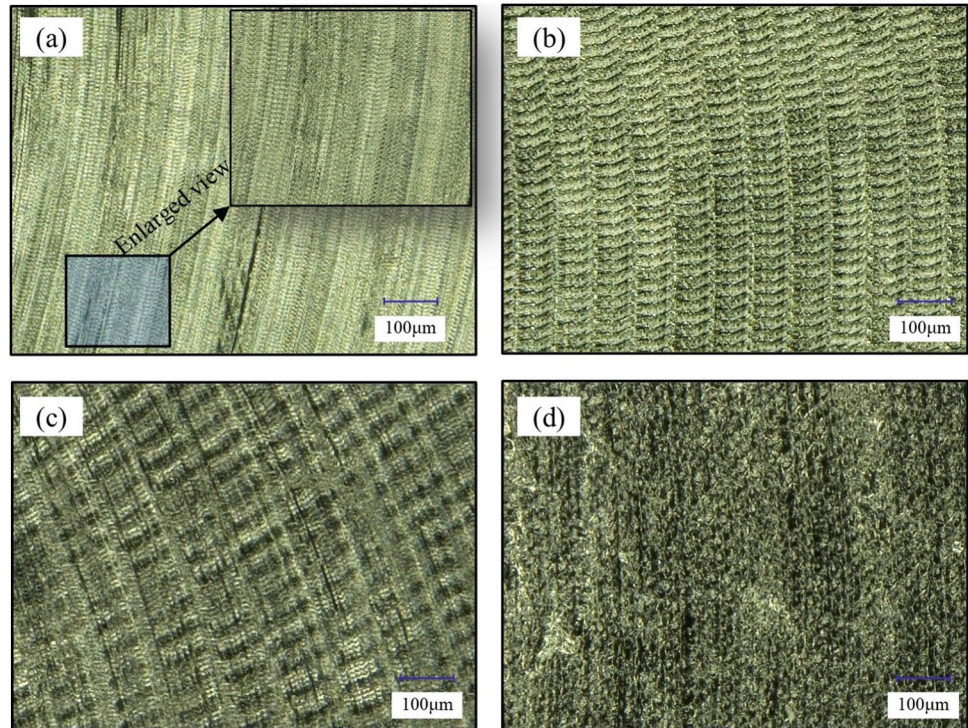
can alleviate these problems. Moreover, the pulsed impact causes the cutting edge to generate a large instantaneous acceleration under a small displacement. The material may become relatively soft, allowing for easy plastic flow. Unlike thermal softening effects, this pattern can reduce the risk of adhesive chips. Accordingly, these machined surfaces of LTUAM have not seen large adhesive chips.

All experimental results in Fig. 11 were based on the same cutting parameters except for the vibration amplitudes ($n = 1700 \text{ r/min}$, $f_r = 0.01 \text{ mm/r}$). Compared with Fig. 11(a), the adhesive chips were improved to some extent at the amplitudes $A_t = 1 \mu\text{m}$, $A_t = 0.67 \mu\text{m}$. However, the surface micro-texture was not obvious. Besides, material elastic recovery should be considered. As a result of these factors, both tool scratches and micro-texture coexisted, as shown in Fig. 11(b). When the amplitude increased $A_t = 3 \mu\text{m}$, $A_t = 1.8 \mu\text{m}$. The stronger the ironing effect, the greater the amplitudes of the vibrations. As a result, the uniform surface

microtexture appeared, and the adhesive chips almost disappeared.

The discrepancy between the experiment and the FEM of the surface microtexture is shown in Fig. 11(e). It proved that the ironing of the tool flank face along the EM trajectory was connected to the creation of microtexture. This is consistent with the analysis of Section 2.3. Yet, as the amplitude increased more, the micro-texture became worse. It can be seen that overgrowing amplitude did not help to cut. FEM confirmed the large slope of micro-texture resulting from the ironing degree over to make them seem as not obvious. Furthermore, the ultrasonic generator applied automatic frequency tracking so that adjusting the output amplitudes may result in a frequency shift. Even if it can output higher power, its stability requires extra attention because the frequency shifted out of the designed resonant frequency band. As illustrated in Fig. 11(d), this results in poor microtexture homogeneity.

Fig. 12 Surface micro-texture of LTUAM with different spindle speeds (in $A_1=3\ \mu\text{m}$, $A_1=1.8\ \mu\text{m}$), (a) $n=1000\ \text{r/min}$; (b) $n=1700\ \text{r/min}$; (c) $n=2400\ \text{r/min}$; (d) $n=3100\ \text{r/min}$



In terms of spindle speeds, the surface micro-texture was varied as shown in Fig. 12. At 1000 r/min, the micro-texture was closely arranged and evenly distributed. It can keep a relatively stable state when the spindle speed increased within a certain range. However, the high speed led the cutting temperature to rise, resulting in adhesive chips and severe tool wear. As expected, when the speed increased, fewer vibration components per unit cutting distance resulted in less micro-texture but larger sizes. As the

speed reached 3100 r/min, they became fairly poor, as seen in Fig. 12(d).

4.2 Surface roughness

Figure 13 presents the influence of vibration amplitudes and spindle speeds on the surface roughness R_a . Compared with CM, the overall surface roughness in LTUAM was decreased. The intervention of vibration was in favor

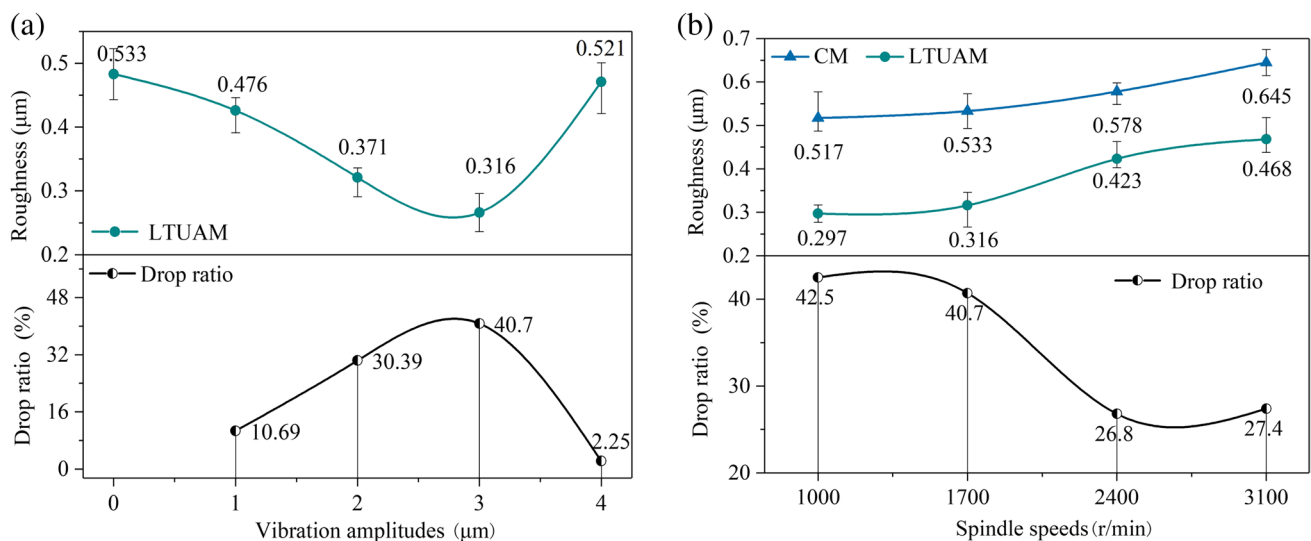


Fig. 13 Surface roughness varied with processing parameters, (a) vibration amplitudes; (b) spindle speeds

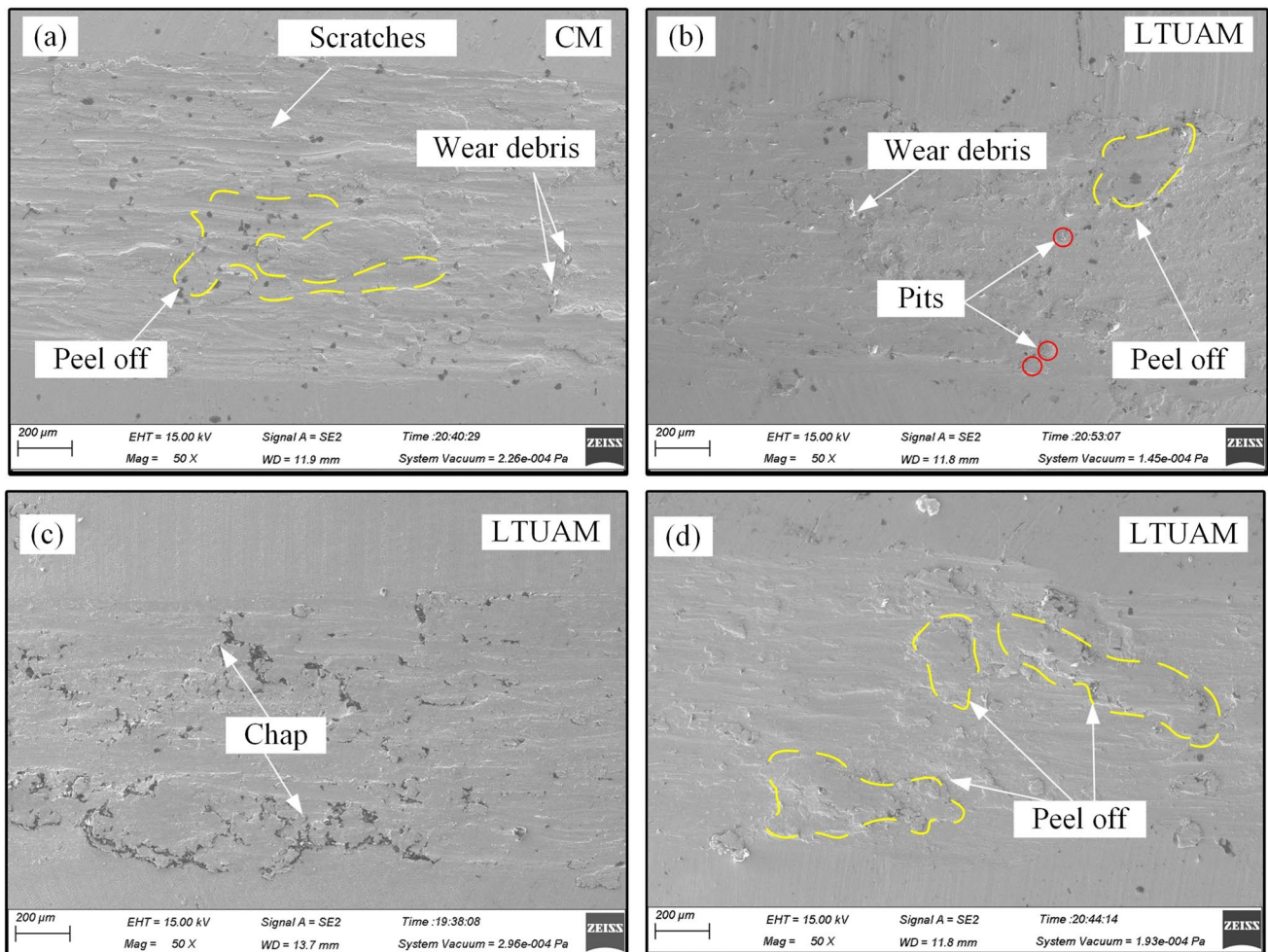


Fig. 14 Wear surface topographies both in CM and LTUAM ($n=1700$ r/min): (a) CM; (b) LTUAM, $A_1=1 \mu\text{m}$, $A_1=0.67 \mu\text{m}$; (c) LTUAM, $A_1=3 \mu\text{m}$, $A_1=1.8 \mu\text{m}$; (d) LTUAM, $A_1=4 \mu\text{m}$, $A_1=3.2 \mu\text{m}$

of cutting material. The surface adhesive impurities were greatly decreased, as were the cutting force and temperature. The minimum value R_a was only $0.316 \mu\text{m}$ et al. = $3 \mu\text{m}$, $A_1=1.8 \mu\text{m}$, with a drop ratio of 40.7% high than in CM. While the amplitudes reached $A_1=4 \mu\text{m}$, $A_1=3.2 \mu\text{m}$, R_a was abruptly increased, and the drop ratio was only 2.25%. It was considered as the impurities on the machined surface, such as adhesive chips.

Concerning the spindle speeds, R_a value in LTUAM was less than CM in all tests. The variation trends, both in CM and LTUAM, increased with the growing spindle speed. The ultrasonic effect was strong at 1000 r/min; thus, the size of the surface micro-texture was small and uniform, resulting in a lower surface roughness of $0.297 \mu\text{m}$. However, the increasing spindle speed significantly reduced the vibration component. The ultrasonic effect weakened, causing the R_a value processively approach CM. The drop ratio was reduced by 35.5% as the spindle speed increased from 1000 to 3100 r/min. To improve surface morphology and roughness, the

amplitude output stability and cutting speed should be carefully evaluated.

Additionally, the micro-texture itself has a certain height difference. R_a may possibly increase even in the better-machined surface state, regardless of contaminants. But it also does not mean that the surface quality was deteriorating. Therefore, more perspectives are needed to evaluate the surface condition of the ultrasonic micro-texture.

4.3 Wear morphologies of machined surfaces

Dry friction and wear experiments were carried out on the machined surfaces to investigate the tribological properties of different micro-textures. The friction mode was reciprocating linear friction, with a friction displacement of 5 mm. The friction pressure was 20 N, and the friction time was 600 s.

The wear morphologies are presented in Fig. 14 after rubbing on the machined surface. The surface wear of

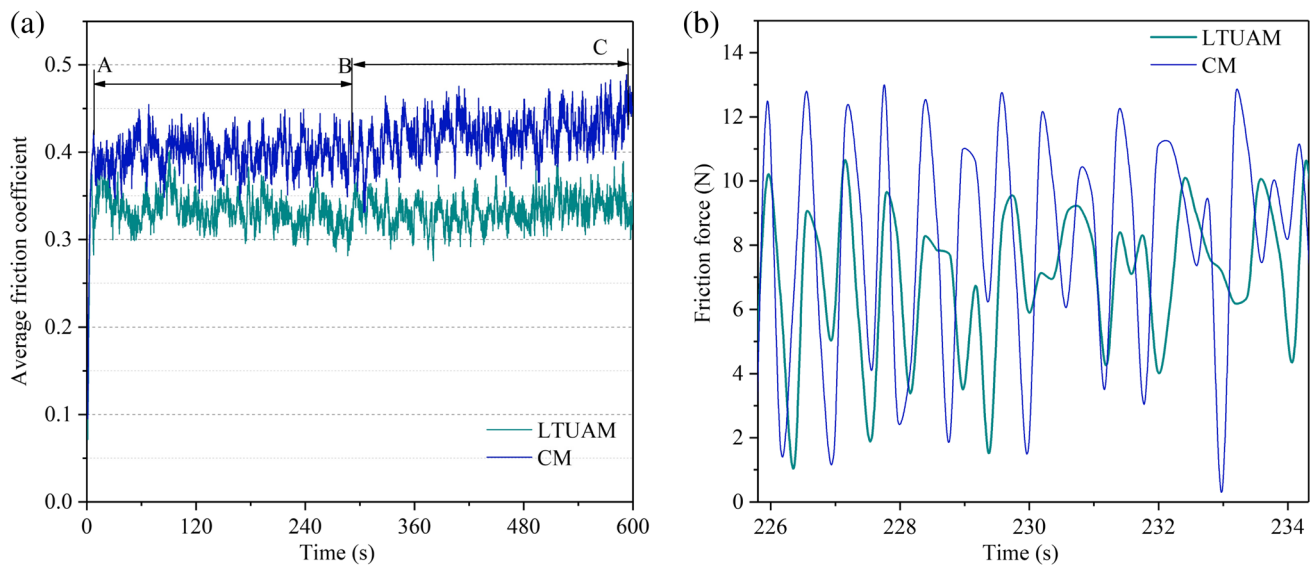


Fig. 15 Tribological properties both in CM and LTUAM ($n=1700$ r/min, $A_1=3$ μm , $A_t=1.8$ μm), (a) average friction coefficient both in CM and LTUAM; (b) friction force both in CM and LTUAM

varying degrees can be noticed. Figure 14(a) depicted peel-off, wear debris, and significant scratches. Nonetheless, the micro-textured surface improved chip-holding capability to some extent. It contributed to reducing the actual contact area between friction pairs, which can reduce friction resistance. Especially the surface obtained in $A_1=3$ μm , $A_t=1.8$ μm , the wear debris and peel off were reduced. Only occurred the material surface chapped, which can be regarded as the feature of the stable wear stage.

The average friction coefficient and friction force help to understand what happens during the friction process (in 1700 r/min). As the friction pair begins to act, the average friction coefficient curve rapidly increases from zero, as seen in Fig. 15. Because of the varying wear resistance of the material surface, the increase rate of the friction coefficient

varied. LTUAM has a lower friction coefficient than CM. In addition, the stable wear stage of CM was shorter than LTUAM, only from A to B. During stage BC, the wear state changed from stable friction to severe, increasing the average friction coefficient. For LTUAM, the friction coefficient was still stable. It indicated that the surface under LTUAM could improve the wear resistance, thus prolonging the stable wear period.

In terms of the friction force, it mainly results from the plough effect and adhesion effect. In CM, the average value was 8.73 N, but in LTUAM, it was 6.22 N. The greater the friction coefficient, the greater the friction force. Increased friction force causes the friction coefficient to fluctuate, reducing the stability period of friction and bringing it into the severe friction stage sooner. In addition, the larger

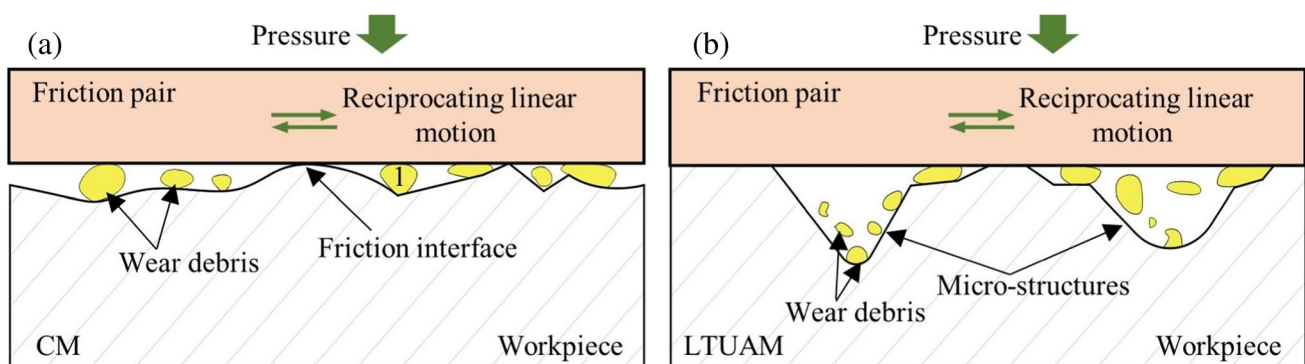


Fig. 16 Schematic diagram of the friction process with different surface types, (a) CM; (b) LTUAM

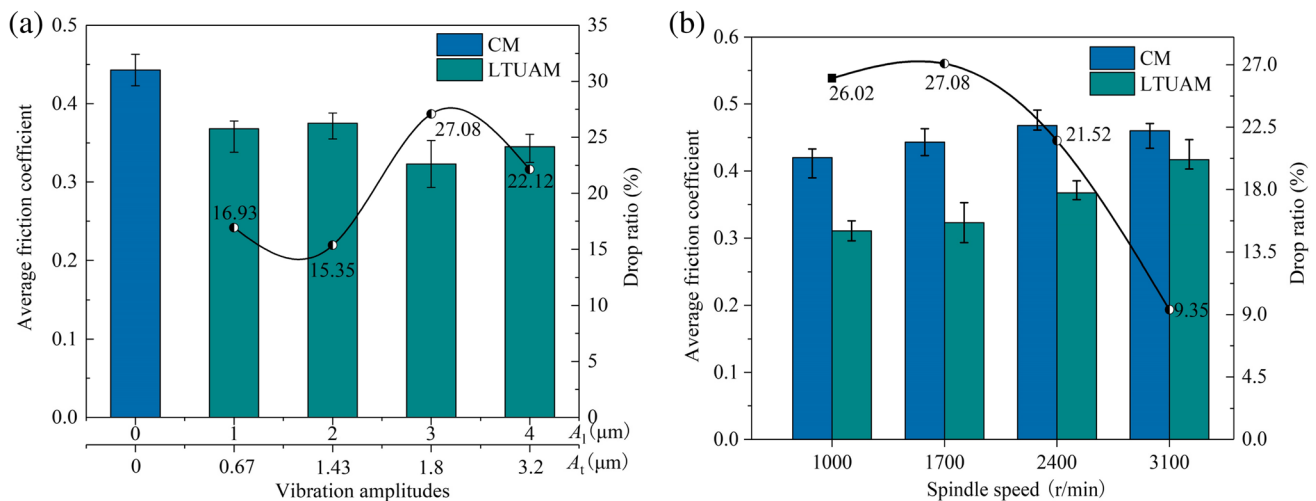


Fig. 17 Average friction coefficients varied with machining parameters, (a) vibration amplitudes; (b) spindle speeds

friction force was related to the fluctuation profile height of CM [10]. More adhesive chips caused it in the machined surface.

4.4 Tribological properties

Figure 16 depicts the friction process of various surfaces. One obvious point is that the machined surface with micro-texture has a particular chip retaining capacity. As certain wear particles or impurities inserted the micro-texture, they improved the contact with the friction pairs, thus suppressing the wear. For those conventional surfaces, occasionally, the plough effect occurred. Under sufficient pressure, irregular debris particles may remove the machined surface. For example, the No. 1 particle is embedded in the surface so that it extrudes the machined surface at a negative rake angle, as shown in Fig. 16(a). So as to cause some pits to occur on the material surface, even peel off especially for larger particles. The fallen debris is held as much as possible in the micro-texture pits to avoid secondary friction during the reciprocating linear friction. There is less debris at the friction interface. As a result, the wear process can maintain a more stable index of LTUAM than CM.

The cutting operation considerably impacted the average friction coefficients in Fig. 17. The average friction coefficient reached a minimum value, only 0.323 in $n = 1700$ r/min, $A_1 = 3 \mu\text{m}$, $A_t = 1.8 \mu\text{m}$. The drop ratio was lower 27.08% than that in CM, while the maximum coefficient occurred et al. = $2 \mu\text{m}$, $A_t = 1.43 \mu\text{m}$. The variation mechanism of the average friction coefficient under different surfaces may be studied by combining Fig. 11. Poor micro-texture morphologies can be seen when the amplitude was low. The effect of ultrasound is not significant. Hence, some chips sticking on the machined surface were still observed easily. Those

surfaces have very little wear resistance. It demonstrated desirable wear resistance for those uniform micro-textures. Its friction coefficient was not only low, but also consistent during the wear process, while the overgrowing vibration amplitudes did not mean a better surface micro-texture. It can be seen the wear resistance was mediocre et al. = $4 \mu\text{m}$, $A_t = 3.2 \mu\text{m}$.

Whether the CM or LTUAM, the average friction coefficient increased gradually as spindle speeds increased. At $n = 1000$ r/min, the friction coefficient of the CM surface was a minimum of 0.42, and LTUAM was 0.31. Increasing spindle speeds linearly increases the material removal rate thereby a large amount of cutting heat is generated, resulting in cutting temperature growth. For Ti_2AlNb , low thermal conductivity limited the chip to take more cutting heat away. As a result, various temperatures accumulated in the cutting zone, subjecting the tool to extreme mechanical and thermal loads. Also, the tool wore heavy. Shear removal is partially converted to extrusion because of the worn cutting edge. And more chips may perhaps adhere to the machined surface, resulting in poor surface quality. Such surfaces fail to achieve desirable frictional performance. At 2400 r/min, the friction coefficient was 0.468, growing 10.25% compared to 1000 r/min. At 3100 r/min, however, the friction coefficient did not rise in CM. The thermal softening effect caused by high cutting speeds is thought to increase Ti_2AlNb machinability. For LTUAM, the work of vibration did not allow the temperature to reach this condition. As a result, the friction coefficient continues to rise. In general, the overall friction coefficients of LTUAM were all lower than CM. Consequently, the surface with a specific micro-texture can improve wear resistance.

5 Conclusions

The study used LTUAM to evaluate the generation mechanism and tribology performance of Ti₂AlNb surface micro-texture. The kinematic features were further investigated, and the finite element model was used to validate their effect on the micro-texture. Milling experiment results supported these conclusions. Tribological tests were also performed on these surfaces with varying micro-texture. The following are the primary conclusions:

- (1) Many feature points were thoroughly addressed during one vibration period, primarily the cut-in, cut-out, switching, and balance points. The critical condition of the separated EM trajectory was proposed on this basis.
- (2) The FEM model of LTUAM Ti₂AlNb discovered that spindle speed mostly affected the density of micro-texture per cutting distance, whereas vibration amplitudes influenced the ability of the cutting edge to iron the workpiece. But the overgrowing amplitudes resulted in excessive ironing so that the micro-texture was seen as smaller.
- (3) The uniform microtexture dominated the machined surface in LTUAM, whereas scratches and adhesive chips dominated in CM. Increasing vibration amplitudes was beneficial for the formation of micro-texture. It only worked well when the vibration was output in a stable resonance band. Roughness results showed a minimum LTUAM of 0.297, a maximum drop ratio of 42.5% in $n = 1000$ r/min, $A_1 = 3$ μm , and $A_t = 1.8$ μm . Raising spindle speeds lowered the vibration component greatly, reducing the influence of vibration. As a result, as the cutting speed increased, the difference in R_a between CM and LTUAM became smaller.
- (4) Surfaces with micro-texture exhibited greater wear resistance. The longer stable phase of the friction curve and lower frictional forces reflected this. LTUAM has less wear debris and peel off state when compared to CM. The minimum average friction coefficient, only 0.323, was obtained in $n = 1700$ r/min, $A_1 = 3$ μm , $A_t = 1.8$ μm , and a maximum drop ratio of 27.08%.

Acknowledgements The authors deeply acknowledge the Key Laboratory of High Performance Manufacturing for Aero Engine (Northwestern Polytechnical University) and Engineering Research Center of Advanced Manufacturing Technology for Aero Engine (Northwestern Polytechnical University) for providing us with the ability to conduct this research.

Author contribution Ziwen Xia: methodology, validation, data curation, writing — original draft. Guofu Gao: conceptualization, methodology, software, writing — original draft. Yi Wang: visualization, investigation. Menghua Zhang: visualization, investigation. Fangchao Jia: conceptualization, methodology, supervision. Chenwei Shan: supervision, funding acquisition, writing — review and editing.

Funding This work was co-supported by the National Natural Science Foundation of China (Nos. 91960203 and 51875473), and the Science Center for Gas Turbine Project (P2022-A-IV-001–002).

Data availability The datasets analyzed during the current study are available from the corresponding author on reasonable request.

Declarations

Ethics approval This paper does not include any research conducted by any author with humans or animals as participants.

Competing interests The authors declare no competing interests.

Consent to participate Not applicable.

Consent for publication Not applicable.

References

1. Zhang HY, Yan N, Liang HY, Liu YC (2021) Phase transformation and microstructure control of Ti₂AlNb-based alloys: a review. *J Mater Sci Technol* 80:203–216. <https://doi.org/10.1016/j.jmst.2020.11.022>
2. Gao GF, Fu ZX, Wang Y, Xiang DH, Zhao B (2021) Research progress on precision machining of Ti-Al intermetallic compounds. *Rare Metal Mat Eng* 50(5):1867–1882
3. Kumpfert J (2001) Intermetallic alloys based on orthorhombic titanium aluminide. *Adv Eng Mater* 3(11):851–864. [https://doi.org/10.1002/1527-2648\(200111\)3:11%3c851::AID-ADEM851%3e3.0.CO;2-G](https://doi.org/10.1002/1527-2648(200111)3:11%3c851::AID-ADEM851%3e3.0.CO;2-G)
4. Hua K, Wan Q, Tong YL, Yang G, Wu HX, Zhou Q, Wang HF (2021) Microstructural feature dependence of dry sliding wear behaviors in a γ -TiAl alloy. *Wear* 484:204039. <https://doi.org/10.1016/j.wear.2021.204039>
5. Zou HB, Yan S, Shen T, Wang HJ, Li Y, Chen JY, Meng YQ, Men SC, Zhang ZJ, Sui TY, Lin B (2021) Efficiency of surface texturing in the reducing of wear for tests starting with initial point contact. *Wear* 482:203957. <https://doi.org/10.1016/j.wear.2021.203957>
6. Li S, Zhang N, Yang ZH, Li X, Zhao G, Wang TM, Wang QH, Zhang XR (2019) Tailoring friction interface with surface texture for high-performance ultrasonic motor friction materials. *Tribol Int* 136:412–420. <https://doi.org/10.1016/j.triboint.2019.03.072>
7. Etsion I (2005) State of the art in laser surface texturing. *J Tribol-T Asme* 127(1):248–253. <https://doi.org/10.1115/1.1828070>
8. Costa HL, Hutchings IM (2009) Development of a maskless electrochemical texturing method. *J Mater Process Tech* 209(8):3869–3878. <https://doi.org/10.1016/j.jmatprotec.2008.09.004>
9. Hua M, Tam HY, Ma HY, Mok CK (2006) Patterned PVD TiN spot coatings on M2 steel: tribological behaviors under different sliding speeds. *Wear* 260(11):1153–1165. <https://doi.org/10.1016/j.wear.2005.07.014>
10. Zhu LD, Ni CB, Yang ZC, Liu CF (2019) Investigations of micro-textured surface generation mechanism and tribological properties in ultrasonic vibration-assisted milling of Ti–6Al–4V. *Precis Eng* 57:229–243. <https://doi.org/10.1016/j.precisioneng.2019.04.010>
11. Liu XF, Zhang JH, Hu XY, Wu DB (2019) Influence of tool material and geometry on micro-textured surface in radial ultrasonic vibration-assisted turning. *Int J Mech Sci* 152:545–557. <https://doi.org/10.1016/j.ijmecsci.2019.01.027>

12. Amini S, Hosseinabadi HN, Sajjadi SA (2016) Experimental study on effect of micro textured surfaces generated by ultrasonic vibration assisted face turning on friction and wear performance. *Appl Surf Sci* 390:633–648. <https://doi.org/10.1016/j.apsusc.2016.07.064>
13. Yang ZC, Zhu LD, Zhang GX, Ni CB, Lin B (2020) Review of ultrasonic vibration-assisted machining in advanced materials. *Int J Mach Tool Manu* 156:103594. <https://doi.org/10.1016/j.ijmactools.2020.103594>
14. Chen F, Bie WB, Wang XB, Zhao B (2022) Longitudinal-torsional coupled rotary ultrasonic machining of ZrO₂ ceramics: an experimental study. *Ceram Int* 48(19):28154–28162. <https://doi.org/10.1016/j.ceramint.2022.05.398>
15. Gao GF, Xia ZW, Yuan ZJ, Xiang DH, Zhao B (2021) Influence of longitudinal-torsional ultrasonic-assisted vibration on micro-hole drilling Ti-6Al-4V. *Chinese J Aeronaut* 34(9):247–260. <https://doi.org/10.1016/j.cja.2020.06.012>
16. Liu YH, Geng DX, Shao ZY, Zhou ZH, Jiang XG, Zhang DY (2021) A study on strengthening and machining integrated ultrasonic peening drilling of Ti-6Al-4V. *Mater Design* 212:110238. <https://doi.org/10.1016/j.matdes.2021.110238>
17. Peng ZL, Zhang XY, Zhang DY (2021) Performance evaluation of high-speed ultrasonic vibration cutting for improving machinability of Inconel 718 with coated carbide tools. *Tribol Int* 155:106. <https://doi.org/10.1016/j.triboint.2020.106766>
18. Zhang ML, Zhang DY, Geng DX, Shao ZY, Liu YH, Jiang XG (2020) Effects of tool vibration on surface integrity in rotary ultrasonic elliptical end milling of Ti-6Al-4V. *J Alloy Compd* 821:153266. <https://doi.org/10.1016/j.jallcom.2019.153266>
19. Xi XX, Yu TY, Ding WF, Xu JH (2018) Grinding of Ti₂AlNb intermetallics using silicon carbide and alumina abrasive wheels: tool surface topology effect on grinding force and ground surface quality. *Precis Eng* 53:134–145. <https://doi.org/10.1016/j.precisioneng.2018.03.007>
20. Wang B, Liu ZQ, Cai YK, Luo XC, Ma HF, Song QH, Xiong ZH (2021) Advancements in material removal mechanism and surface integrity of high speed metal cutting: a review. *Int J Mach Tool Manu* 166:103744. <https://doi.org/10.1016/j.ijmactools.2021.103744>
21. He LJ, Su HH, Xu JH, Zhang L (2018) Inverse identification of constitutive parameters of Ti₂AlNb intermetallic alloys based on cooperative particle swarm optimization. *Chinese J Aeronaut* 31(8):1774–1785. <https://doi.org/10.1016/j.cja.2018.01.002>
22. Xi XX, Ding WF, Fu YC, Xu JH (2018) Grindability evaluation and tool wear during grinding of Ti₂AlNb intermetallics. *Int J Adv Manuf Tech* 94(1–4):1441–1450. <https://doi.org/10.1007/s00170-017-1005-7>
23. Sim KH, Zhang FH, Wang GF, Rao XS (2018) Experimental comparison of ground surface characteristics for P/M Ti₂AlNb-based alloy using CBN and diamond grinding wheels. *Int J Adv Manuf Tech* 94(5–8):1885–1894. <https://doi.org/10.1007/s00170-017-0900-2>
24. Yuan ZJ, Gao GF, Wang Y, Fu ZX, Xiang DH (2022) Correction to: Experimental study on a two-dimensional ultrasonic vibration platform and milling of Ti₂AlNb intermetallic alloy. *Int J Adv Manuf Tech* 122(5):2793–2793. <https://doi.org/10.1007/s00170-022-10130-5>
25. Bhaduri D, Soo SL, Aspinwall DK, Novovic D, Bohr S, Harden P, Webster JA (2017) Ultrasonic assisted creep feed grinding of gamma titanium aluminide using conventional and superabrasive wheels. *Cirp Ann-Manuf Techn* 66(1):341–344. <https://doi.org/10.1016/j.cirp.2017.04.085>
26. Buchkremer S, Wu B, Lung D, Münstermann S, Klocke F, Bleck W (2014) FE-simulation of machining processes with a new material model. *J Mater Process Tech* 214(3):599–611. <https://doi.org/10.1016/j.jmatprotec.2013.10.014>
27. Zhao B, Guo XC, Bie WB, Chang BQ, Zhao CY (2020) Thermo-mechanical coupling effect on surface residual stress during ultrasonic vibration-assisted forming grinding gear. *J Manuf Process* 59:19–32. <https://doi.org/10.1016/j.jmapro.2020.09.041>
28. Mahnama M, Movahhedy MR (2012) Application of FEM simulation of chip formation to stability analysis in orthogonal cutting process. *J Manuf Process* 14(3):188–194. <https://doi.org/10.1016/j.jmapro.2011.12.007>
29. Xu J, He L, Su H, Zhang L (2018) Tool wear investigation in high-pressure jet coolant assisted machining Ti₂AlNb intermetallic alloys based on FEM. *Int J Light Mater Manuf* 1(4):219–228. <https://doi.org/10.1016/j.ijlmm.2018.08.007>
30. Bai W, Wang K, Du DX, Zhang JG, Huang W, Xu JF (2022) Design of an ultrasonic elliptical vibration device with two stationary points for ultra-precision cutting. *Ultrasonics* 120:106662. <https://doi.org/10.1016/j.ultras.2021.106662>
31. Jung HJ, Hayasaka T, Shamoto E, Xu LJ (2020) Suppression of forced vibration due to chip segmentation in ultrasonic elliptical vibration cutting of titanium alloy Ti-6Al-4V. *Precis Eng* 64:98–107. <https://doi.org/10.1016/j.precisioneng.2020.03.017>
32. Li X, Zhang DY (2010) Experimental study on the unseparated ultrasonic elliptical vibration cutting. *Chin J Mech Eng-En* 46(19):177–182. <https://doi.org/10.3901/JME.2010.19.177>
33. Zhao B, Bie WB, Wang XB, Chang BQ (2020) Design and experimental investigation on vibration system of longitudinal-torsional ultrasonic drilling TC4 titanium alloy. *Acta Aeronautica et Astronautica Sinica* 41(1):291–303. <https://doi.org/10.7527/S1000-6893.2019.23207>

Publisher's note Springer Nature remains neutral with regard to jurisdictional claims in published maps and institutional affiliations.

Springer Nature or its licensor (e.g. a society or other partner) holds exclusive rights to this article under a publishing agreement with the author(s) or other rightsholder(s); author self-archiving of the accepted manuscript version of this article is solely governed by the terms of such publishing agreement and applicable law.